

# Modulation of Cathodoluminescence by Surface Plasmons in Silver Nanowires

Amelia C. Y. Liu,\* Timothy J. Davis,\* Toon Coenen, Sangeetha Hari, Lenard M. Voortman, Zhou Xu, Gangcheng Yuan, Patrycja M. Ballard, Alison M. Funston, and Joanne Etheridge

The waveguide modes in chemically-grown silver nanowires on silicon nitride substrates are observed using spectrally- and spatially-resolved cathodoluminescence (CL) excited by high-energy electrons in a scanning electron microscope. The presence of a long-range, travelling surface plasmon mode modulates the coupling efficiency of the incident electron energy into the nanowires, which is observed as oscillations in the measured CL with the point of excitation by the focused electron beam. The experimental data are modeled using the theory of surface plasmon polariton modes in cylindrical metal waveguides, enabling the complex mode wavenumbers and excitation strength of the long-range surface plasmon mode to be extracted. The experiments yield insight into the energy transfer mechanisms between fast electrons and coherent oscillations in surface charge density in metal nanowires and the relative amplitudes of the radiative processes excited in the wire by the electron.

applications, from sensing, trapping, and tweezing, to communications and signaling, and to lasers and optical displays.<sup>[5]</sup> Nanoplasmonics, in particular, offers a route for controlling light at length scales below the optical diffraction limit.<sup>[6]</sup> These materials consist of nanoscale metallic or dielectric structures that trap light at a surface or interface. This trapped light may propagate as a surface plasmon-polariton (SPP) or charge density wave, until it is scattered at a discontinuity in refractive index to the far-field as light. In confined structures, the SPP may form a localized surface plasmon resonance (LSPR) and radiate light with energies and directions that reflect the size and symmetry of the nanostructure.


Understanding how these nanoscale materials harness and radiate light is critical to tailoring their properties for particular applications. Focused high-energy electron beams in the scanning/transmission electron microscope (S/TEM) and scanning electron microscope (SEM) offer unique potential capability to characterize these materials at their natural length scale due to the

## 1. Introduction

Nanophotonic materials are a unique way to modify the color,<sup>[1]</sup> amplitude and phase,<sup>[2]</sup> polarization,<sup>[3]</sup> direction, and spatial distribution of light.<sup>[4]</sup> These materials have a large number of

A. C. Y. Liu, J. Etheridge  
School of Physics and Astronomy  
Monash University  
Clayton, Victoria 3800, Australia  
E-mail: amelia.liu@monash.edu  
A. C. Y. Liu, Z. Xu, J. Etheridge  
Monash Centre for Electron Microscopy  
Monash University  
Clayton, Victoria 3800, Australia

T. J. Davis  
School of Physics  
University of Melbourne  
Parkville, Victoria 3010, Australia  
E-mail: timd@unimelb.edu.au  
T. Coenen, S. Hari, L. M. Voortman  
Delmic BV  
Kanaalweg 4, Delft 2628 EB, The Netherlands  
L. M. Voortman  
Division of Cell and Chemical Biology  
Leiden University Medical Centre  
Leiden University  
Leiden 2333 ZC, The Netherlands  
G. Yuan, P. M. Ballard, A. M. Funston  
ARC Centre of Excellence in Exciton Science and School of Chemistry  
Monash University  
Clayton, Victoria 3800, Australia  
J. Etheridge  
Department of Materials Science and Engineering  
Monash University  
Clayton, Victoria 3800, Australia

 The ORCID identification number(s) for the author(s) of this article can be found under <https://doi.org/10.1002/smll.202207747>.

© 2023 The Authors. Small published by Wiley-VCH GmbH. This is an open access article under the terms of the Creative Commons Attribution-NonCommercial-NoDerivs License, which permits use and distribution in any medium, provided the original work is properly cited, the use is non-commercial and no modifications or adaptations are made.

DOI: 10.1002/smll.202207747

truly nanoscale, local nature of excitation with the focused electron beam and the broadband nature of electron excitation.<sup>[7–11]</sup>

Electron energy loss spectroscopy (EELS) in the S/TEM is an extremely valuable technique for studying the excitation of SPPs in metal nanostructures. Fast electrons that are transmitted near or through the metal surface lose energy by several processes<sup>[12,13]</sup> one of which is the excitation of SPPs or LSPRs. The probability of electron energy loss to surface plasmon excitations is spatially modulated as observed by scanning the focused electron beam across the nanostructure. This modulated EELS probability is directly related to the optical local density of states<sup>[14]</sup> projected along the electron beam direction.<sup>[12,15]</sup> This interpretation has facilitated understanding of LSPRs in 2D metal plates,<sup>[16]</sup> 3D nanoparticles,<sup>[17]</sup> and 1D metal wires<sup>[18–22]</sup> and travelling SPPs in longer wires.<sup>[23]</sup> EELS of wires has measured SPP dispersion curves and studied SPP propagation in more complex wire geometries.<sup>[20,22,23]</sup>

The interaction of the electron beam with a metallic nanostructure also can result in light emission, known as cathodoluminescence (CL), which can be collected in a S/TEM or SEM.<sup>[7,11]</sup> The passage of a fast electron across a dielectric interface, such as the vacuum-metal boundary, results in the emission of light,<sup>[12,13]</sup> known as transition radiation, that arises from the rapid change in the induced electric polarization in the medium.<sup>[24]</sup> This transition radiation, arising from the instantaneous formation of an electric dipole perpendicular to the boundary and direct emission into free space, is the dominant source of cathodoluminescence in fast electron bombardment of smooth, planar metal surfaces. The electric dipole can also launch SPPs that propagate away from the excitation position.<sup>[12]</sup> For a perfect, planar surface, these oscillations will be non-radiating, but for thin foils, rough films, and confined geometries the SPPs may produce radiation.<sup>[25–30]</sup> These forms of coherent CL are also spatially modulated with beam position, explained by an association with the radiative component of the optical or electromagnetic local density of states (LDOS) projected along the electron beam direction.<sup>[16,31]</sup> This association also explains the asymmetric CL lineshapes and resonance energy shifts with respect to EELS,<sup>[31,32]</sup> a common phenomenon for far and near-field peaks from damped harmonic oscillators.<sup>[33]</sup>

In general, the interpretation of EELS and CL data from plasmonic structures relies upon this LDOS interpretation and simple phenomenological wave models (for example the Fabry–Pérot resonators,<sup>[18,20,21,34]</sup> wave interference<sup>[23,35]</sup> or simulation using the boundary element or finite-difference time domain methods to solve Maxwell's equations locally (metallic nanoparticle boundary element method package<sup>[36–38]</sup> or commercial solvers). These approaches can extract some parameters of interest (for example, complex SPP wavevector) and explain the appearance of spectra, but obscure many details of the fast electron interaction, excitation of different processes and subsequent emission of light. Here we develop an analytical electromagnetic model for CL emission from a nanowire with a long-range SPP mode. We test our model against two CL measurements conducted in an SEM: one that measures the spectrally-resolved total CL at different excitation positions and one that spatially resolves the CL emission at different excitation positions. Our model matches both CL measurements extremely well, and considerably advances understanding of the physics

of excitation with an electron beam and competition between different radiative processes. Moreover, this approach can be used to measure many parameters of interest, such as the complex SPP wavevector and the relative excitation amplitude and phase relationship of the long-range SPP compared to radiant processes at the excitation point.

The geometry of the two different CL measurements in SEMs is displayed in **Figure 1**. In the first, more conventional, spectrally-resolved CL measurement (**Figure 1a**), the CL emitted into the upper hemisphere is collected by a parabolic mirror and then focused before being fiber-optically coupled to a spectrometer. CL spectra are collected at different electron probe excitation points as the beam is raster-scanned along the wire.<sup>[9–11]</sup> In the second, spatially-resolved CL measurement shown in **Figure 1b**, the CL emitted by the nanostructure is collected through a transparent substrate (silicon nitride membrane on a silicon support on a glass coverslip) by a high-numerical aperture optical microscope in epi-fluorescence configuration, resolving the position and relative magnitudes of any light emitted due to excitation by the electron probe at different points along the wire. This method was developed for correlative optical-electron imaging of biological structures,<sup>[39]</sup> but here we apply it to light emission from plasmonic nanomaterials. The spatial resolution of the spectrally-resolved measurement is limited by the extent of the evanescent field of the electron beam,  $\approx 20\text{--}30$  nm for 30 keV electrons.<sup>[12]</sup> The resolution of the spatially-resolved CL measurement is limited by the microscope objective numerical aperture and the size of the camera pixels, giving a full-width spot size for a point emitter of approximately 1000 nm. In both CL experiments we studied chemically grown penta-twinned silver nanowires<sup>[40]</sup> with diameters of  $\approx 80$  nm and lengths that ranged from 2–15  $\mu\text{m}$ . These wires were deposited on 50 nm thick silicon nitride membranes from ethanol solutions. An SEM image of a typical, nicely isolated, silver nanowire is displayed in **Figure 1e**. See Experimental Section for further information.

## 2. Results and Discussion

The spectrally-resolved CL is modulated as a function of probe position, having a maximum near the end of the wire, and then undergoing decaying oscillations as a function of increasing distance from the end as we see in **Figure 2a** and intensity profiles of **Figure 2a** at constant freespace wavelength (in Supporting Information). The period of these oscillations is approximately a factor of two smaller than the free-space wavelength, similar to observations of oscillations in EELS intensity from nanowires,<sup>[23,34]</sup> and also CL from strip antennas, groove resonators, and gratings fabricated in metal films.<sup>[35,41,42]</sup> **Figure 2c–f** shows parameters extracted from fits to this data employing our model (detailed below and in the Supporting Information) and **Figure 2b** displays simulated CL using this model.

The spatially-resolved CL measurements (for example the image series in **Figure 3a–d** and **Movie S1**, Supporting Information) demonstrate strikingly the different radiant processes excited by the electron beam. We observe strong light emission from the point of impact of the electron beam and light emission from the ends of the nanowires that increases in intensity

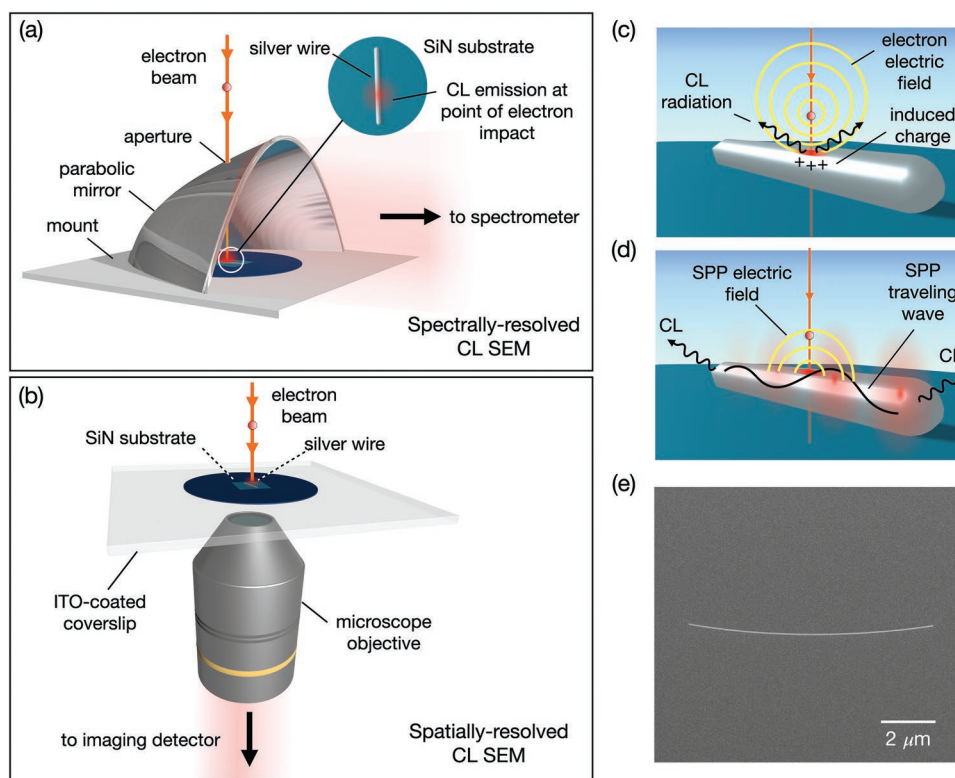


**Figure 1.** SEM-based methods for measuring cathodoluminescence (CL) from silver nanowires on a silicon nitride (SiN) substrate and the interaction mechanisms. a) The spectrally-resolved CL employs a parabolic mirror to collect the emitted light and direct it to a spectrometer. b) The spatially-resolved CL images the CL emission with an optical microscope; note the spatial resolution in (a) is limited by the electric field of the probe, while in (b) the spatial resolution is limited by the optical microscope and camera. c) The evanescent electric field from the incident, fast electron induces electric charges in the metal that result in the emission of CL as well as the formation of a propagating surface plasmon. d) The surface plasmon induced in the nanowire forms a standing wave, the electric field of which interacts back on the electron, modifying the CL radiation. e) SEM image of a typical nanowire.

as the electron beam approaches each respective end. The size of these emission spots is 1000–1100 nm (full-width), consistent with the optical diffraction limit and the pixel size (110 nm). The emission at the electron beam position is predominantly due to coherent CL from the wire, with a small component due to coherent and incoherent CL from the silicon nitride membrane<sup>[43]</sup> and incoherent CL from the glass coverslip that we consider a constant background (Experimental Section and Supporting Information).

The light emission detected from the ends of the wires is a sign of SPP excitation and propagation in the nanowire and light coupling to the far-field at the wire ends. This emission is a factor of approximately one hundred fainter than the CL emitted from the point of excitation, but increases as the point of excitation approaches the end of the wire and damping decreases. We plot the CL intensity at the excitation position and at the ends of the wire, as a function of excitation position,  $z_0$  in Figure 3e,f, respectively. The CL at the point of excitation is constant at most probe positions, except for a marked increase close to the wire ends. The CL from the long-range SPP mode that scatters to the far field at  $z = \pm L/2$  shows a damping behavior consistent with an appreciable imaginary component of the SPP wavevector ( $k_z$ ), especially for smaller wavelengths. Experiments employing optical excitation at one end of a wire with a travelling SPP, also observe propagation, damping, and

emission at the other end<sup>[34,44–48]</sup> and sometimes oscillations with free-space wavelength of the scattered light.<sup>[34,46,48]</sup>

## 2.1. Interaction Model

To understand the spectral and spatial modulation of CL emission as a function of excitation position and wavelength, we develop a simplified model of the interaction between the incident electron and the electric fields induced in the nanowire. The complete model derivation is given in the Supporting Information, with main points summarized here.

The fast electron (here represented by a current density  $\mathbf{J}_e$ ) loses energy ( $\dot{u}$ ) by doing work against an induced electric field  $\mathbf{E}$  (Figure 1c), with the rate of energy loss in a volume  $V$  given by,<sup>[49]</sup>

$$\dot{u} = \frac{1}{2} \int \mathbf{J}_e^* \cdot \mathbf{E} dV \quad (1)$$

In the CL experiment,  $\mathbf{E}$  arises from the redistribution of electric charge in the metal wire, induced by the field of the approaching electron. This charge redistribution can be represented mathematically by a linear combination of orthogonal electromagnetic modes within the wires that are associated with surface charges and electromagnetic fields extending

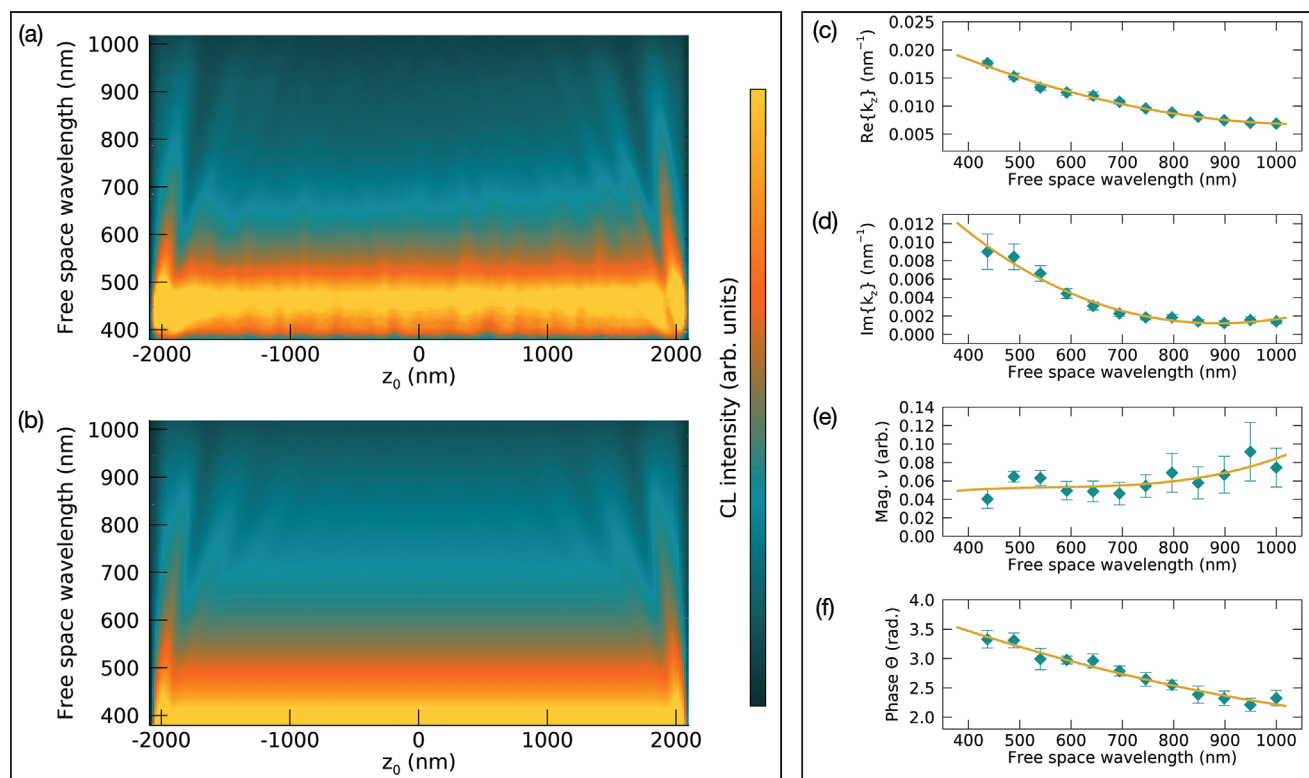


**Figure 2.** Spectrally-resolved CL data as a function of probe position,  $z_0$  for a nanowire with length,  $L = 4.22 \mu\text{m}$ . a) Measured distribution. b) Simulated distribution using the interpolated parameter values (shown in (c–f)) from the model fits (Equation (7)). c–f) Average fitted parameters from fits to the intensity profiles of five wires using the model in Equation (7). The error bars indicate standard errors. Polynomial functions that smoothly interpolate the fitted parameters are overlaid as a solid line. These interpolated values are used to simulate the spectrally-resolved CL as shown in (b).

outside the wire. In this regard we consider these as SPP modes. The lowest order waveguide mode is the long-range SPP mode that can travel to the ends of the wire, reflect, and return to the point of excitation. We use Equation (1) to derive the amplitude of the source for exciting SPP waves with an electron (see Supporting Information). This source term (introduced in Equation (3) below) is modulated by the electric field of the reflected long-range SPP mode, giving rise to the oscillations observed in the spectrally-resolved CL.

We model our wires as metal cylinders or cylindrical waveguides as their diameter is much smaller than the surface plasmon wavelength. The electric and magnetic fields from surface plasmon modes along these wires have been derived previously<sup>[50,51]</sup> with eigenvalue solutions being the wavenumbers  $k_z$  of the modes along the length of the wire with permittivity  $\epsilon_m$ . All but the  $n = 0$  mode is very lossy for the dimensions of wires we investigate. This is a transverse magnetic (TM) mode where only the radial  $E_r(r, z)$  and longitudinal  $E_z(r, z)$  components of the electric field are non-zero. In Figure 4a we show the theoretical dispersion relationship for this  $n = 0$  mode.<sup>[50,51]</sup> Figure 4b illustrates the radial, longitudinal, and azimuthal co-ordinates  $(r, z, \phi)$  and Figure 4c shows the magnitude of the calculated radial and longitudinal electric fields and azimuthal magnetic field in the wire cross-section.

For a wire of very small radius  $a$ , the longitudinal mode is approximately constant over the cross section whereas the radial mode varies linearly with  $r$ . For the 1D case suggested

by this excitation geometry, we average the field over the wire cross section to remove the dependence on  $r$ , giving the approximate solution for the electric field at longitudinal position and time,  $(z, t)$ , as

$$\mathbf{E}(z, t) \approx E_0 (\hat{z} - i\kappa\hat{r}) e^{ik_z z - i\omega t} \quad (2)$$

Here,  $E_0$  is an amplitude and the radial component depends on  $\kappa = k_z a/3$  which changes sign with the direction of propagation  $k_z$ .

The SPP waves are excited by the electron incident at position  $z_0$  along the wire and propagate away from this point. The solution to the 1D wave equation in the presence of a source is

$$\mathbf{E}(z, z_0) = E_+ (\hat{z} - i\kappa\hat{r}) e^{ik_z z} + E_- (\hat{z} + i\kappa\hat{r}) e^{-ik_z z} + S_{\pm} (\hat{z} \mp i\kappa\hat{r}) e^{ik_z |z - z_0|} \quad (3)$$

Here  $\mathbf{E}(z, z_0)$  is the electric field at  $z$  for an excitation position of  $z_0$ .  $E_{\pm}$  are the amplitudes for the forward and backward propagating waves, respectively and  $S_{\pm}$  is the source amplitude that may have a sign or a phase that depends on the direction of propagation away from the point of impact. This equation can be used to model the electric field at the wire ends ( $z = \pm L/2$ , where  $L$  is the wire length) or at the point of excitation  $z = z_0$  as a function of excitation point,  $z_0$ . These modeled distributions can be compared directly to the measured spectrally and spatially-resolved CL from SEM experiments.

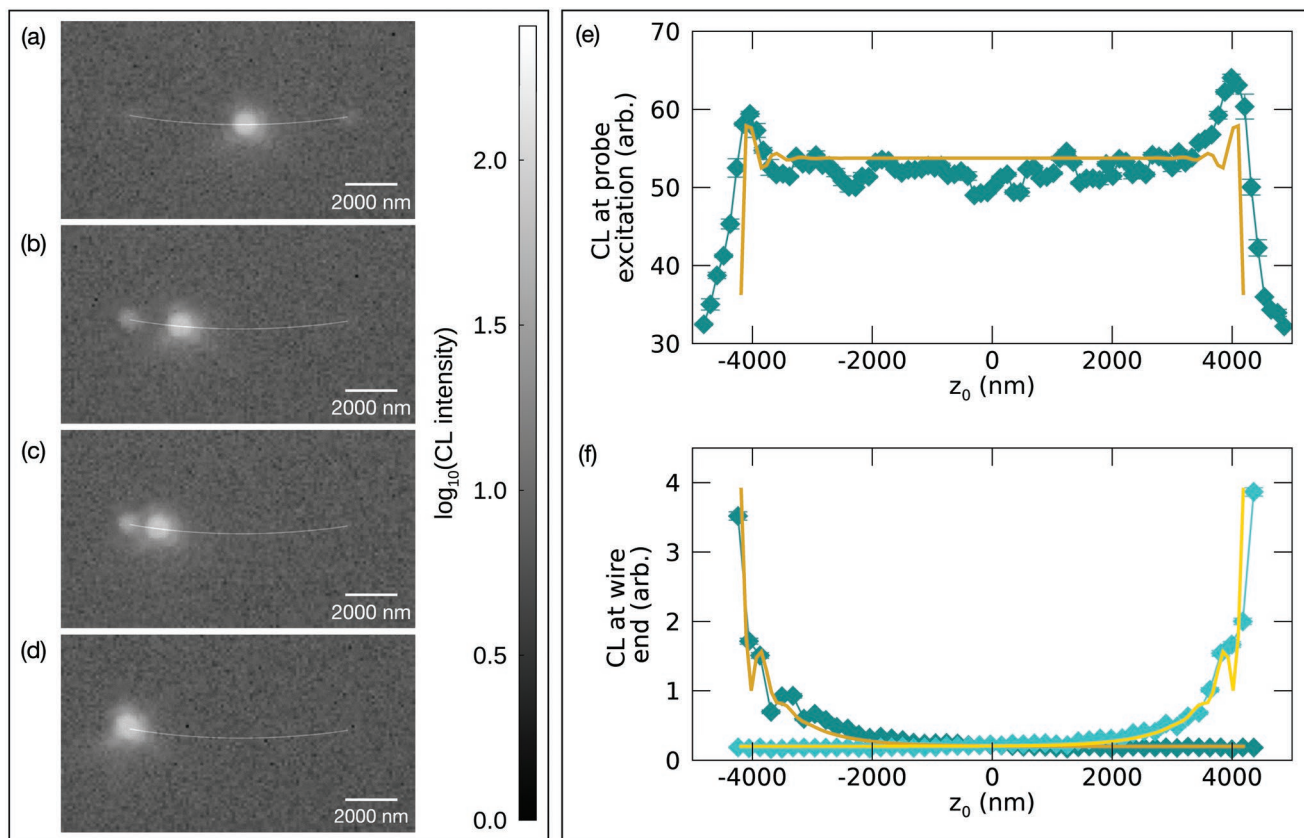


**Figure 3.** Spatially-resolved CL as a function of probe position,  $z_0$ . a–d) Optical images (long-pass filter admitting light above 458 nm) from the spatially-resolved CL measurements with the SEM image of the silver nanowire overlaid. Note that a log scale is employed to highlight faint emission from the ends of the wire. e) CL emitted at the excitation position,  $z_0$ , as a function of  $z_0$ . f) CL emitted at the ends of the wire ( $z = \pm L/2$ ) as a function of  $z_0$ . This CL arises from long-range SPP generation, propagation and scattering to the far-field. In (e) and (f) the CL is divided by 1000 for ease of comparison between the curves and the data are displayed with simulated results overlaid as solid lines, and using the standard deviation of the intensity as error bars. Note in (f) the darker blue symbols and dark yellow line is from the left end of the wire, while the lighter symbols and line corresponds to the CL from the right end. The simulated curves employed parameters derived from fitting the spectrally-resolved measurements with our model.

We employ boundary conditions at the ends of the wire to determine the amplitudes  $E_{\pm}$  and the probable symmetry in the excitation amplitudes  $S_+ = -S_- = S_0(z_0)$  to write the SPP field in the wire in the form

$$\mathbf{E}_{\text{spp}}(z, z_0) = \frac{2iS_0(z_0)e^{ik_z L}}{e^{2ik_z L} - R^2} \left[ (R \sin k_z(z+z_0) - e^{ik_z L} \sin k_z(z-z_0)) \hat{z} + \kappa(e^{ik_z L} \cos k_z(z-z_0) - R \cos k_z(z+z_0)) \hat{r} \right] + S_0(z_0)e^{ik_z|z-z_0|}(\pm \hat{z} - i\kappa \hat{r}) \quad (4)$$

where the + sign is used for  $z > z_0$  and the – sign for when  $z < z_0$ .  $R$  is a reflection coefficient that naturally comes from the application of the boundary conditions (Supporting Information).

We employ Equation (1) which is the starting point for deriving Poynting's theorem and the orthogonality relationship between the radial electric field and the azimuthal magnetic field to derive an expression for the source amplitude as shown below

$$S_0(z_0) = -is_0 \left( \frac{2e^{ik_z L} (e^{ik_z L} - R \cos 2k_z z_0)}{e^{2ik_z L} - R^2} - 1 \right) \quad (5)$$

$s_0$  arises from a group of constant factors and is employed as a fixed parameter to scale the model to the experimental data during fitting.

This expression for the source amplitude oscillates with  $2k_z z_0$  (Equation (5)) illuminating the underlying physics of SPP excitation with energetic electrons and consequent light emission. The electron beam excites both coherent processes at the position of excitation and a long-range zeroth-order travelling SPP. The long-range SPP travels to the wire ends, where it partially reflects and transmits, causing light emission as it scatters to the far-field. The reflected wave modifies the induced electric field at the point of excitation (Figure 1d), giving rise to oscillations in  $S_0(z_0)$  that in turn modulate the excitation of both the emission processes at  $z_0$  and at  $z = \pm L/2$ . This effect is similar to the modification of atomic fluorescence due to the presence of a reflecting surface.<sup>[52–54]</sup> Such effects are well-known in waveguides where the strength of the excitation of a waveguide mode depends on the impedance at the excitation position. This interpretation is also fully consistent with the identification of CL with the radiative LDOS,<sup>[16,31,35]</sup> but in our derivation, the modulation of the source term has arisen naturally from a solution to the 1D wave equation to describe the electric field along the wire.

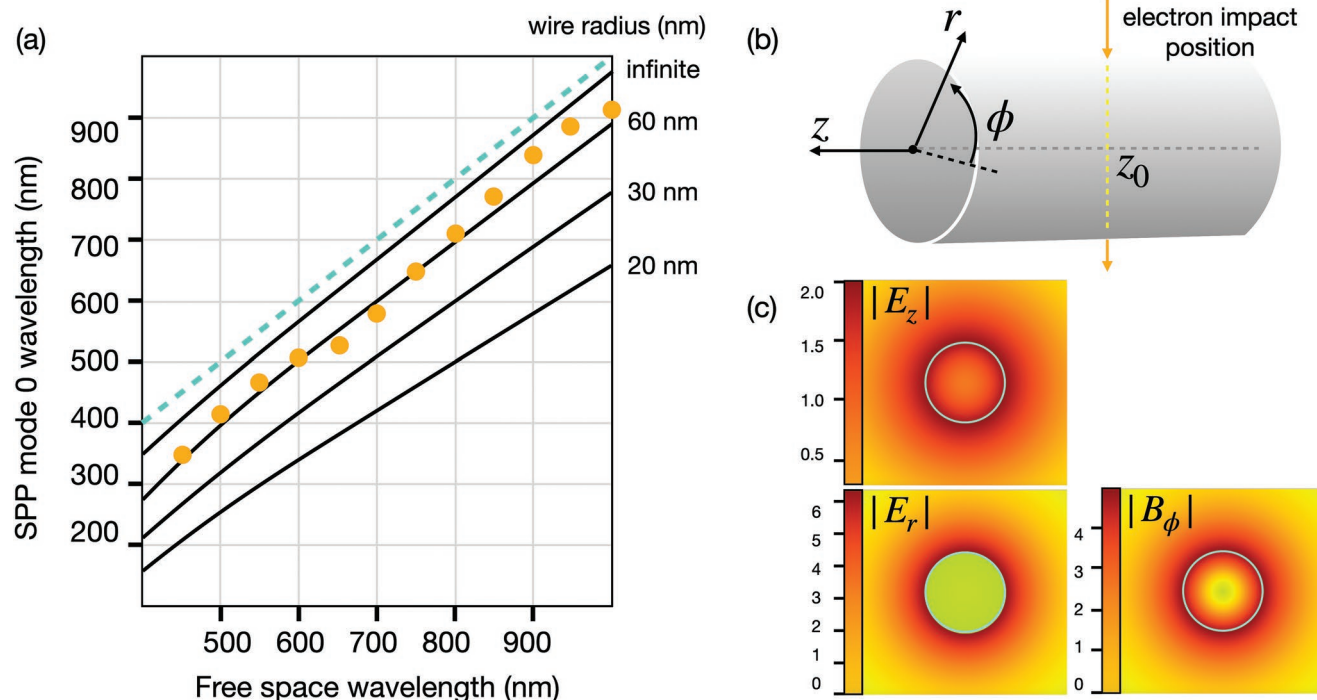


**Figure 4.** Long-range  $n = 0$  SPP modes in a silver nanowire. a) The dispersion relation for the  $n = 0$  SPP mode in a silver wire for different wire radius. The solid lines are theory and the points are results from fits to the spectrally-resolved CL measurements employing our model. The light line is shown as a dashed blue line. b) Radial ( $r$ ), longitudinal ( $z$ ), and azimuthal ( $\phi$ ) directions. c) The calculated magnitudes of the electric and magnetic fields in the wire cross section. All these fields oscillate with distance  $z$  along the wire. The blue circles indicate the surface of the nanowire. Note that the  $E_z$  field oscillates  $90^\circ$  out of phase with respect to  $E_r$  and  $B_\phi$ . All other field components for the  $n = 0$  SPP mode are zero.

To determine the emission at  $z = \pm L/2$  from travelling SPPs, we assume that the longitudinal components of the electric field are responsible for the oscillating surface charge distributions at the wire ends that radiate light.

$$E_{\text{spp}}^{\text{CL}} = \left( \frac{\epsilon_m}{\epsilon_v} \right) \left\{ \hat{z} \cdot [\mathbf{E}_{\text{spp}}(L/2, z_0) - \mathbf{E}_{\text{spp}}(-L/2, z_0)] \right\} \quad (6)$$

where  $\epsilon_v$  is the vacuum permittivity. Finally, the intensity  $I_{\text{CL}}(z_0)$  of the CL radiation from the point of impact of the electron is proportional to the total electric field distribution  $\mathbf{E}_T$  excited in the wire at  $z_0$ . Here  $\mathbf{E}_T$  includes all the processes discussed above that are local solutions to Maxwell's equations, such as transition radiation and SPPs that radiate due to the wire's 3D geometry (Movie S2 Supporting Information).<sup>[12,30]</sup> However the long-range SPP mode does not contribute to the CL at the point of impact, since it is non-radiating, and needs to be subtracted. We hypothesize that the radial component  $\mathbf{E} \cdot \hat{r}$  is the dominant source of this radiation, giving this final expression for  $I_{\text{CL}}(z_0)$ :

$$I_{\text{CL}}(z_0) \propto |E_r(1 - \nu e^{i\Theta} \hat{r} \cdot \mathbf{E}_{\text{spp}}(z_0, z_0))|^2 \quad (7)$$

Here we account for an unknown magnitude  $\nu$  that represents the relative excitation probability of the long range plasmon compared to the radiative processes at the point of excitation and a phase offset,  $\Theta$ , between these two coherent phenomena. We also omit the contribution from the CL at the wire ends as our spatially-resolved measurements show that the end-emission is orders of magnitude weaker than the CL from

the point of impact, and we cannot resolve these contributions in our spectral measurements.

Figure 2a shows the spectrally-resolved data for a  $L = 4.22 \mu\text{m}$  silver wire. Figure 2c–f of the same figure display the averaged parameters from fits employing Equation (7) to the CL intensity profiles of five wires at 50 nm intervals in free-space wavelength (see Experimental Details and Supporting Information for example fits). These extracted values are reasonable. We overlay the dispersion relationship that we obtain from our fit on Figure 4a and find good agreement, validating initial assumptions about the cylindrical geometry. The imaginary part of the SPP wavevector Figure 2d compares well to previous measurements.<sup>[18]</sup> The values of  $\nu$  Figure 2e correctly predict the relative magnitude of the radiative processes we observe in the spatially-resolved measurements.

Figure 2b shows a simulated spectral image as a function of probe excitation position using the average fitted parameters that have been interpolated with polynomials (solid lines in Figure 2c–f). The simulation compares well to the data in Figure 2a, but lacks noise and small features arising from imperfections, as it employs averaged and smoothly interpolated parameter values. The fits and simulations validate our model of the spectrally-resolved CL data from the nanowire. The simulated source modulation, CL emitted at the point of excitation, and the CL emitted from the ends of the wire that match the simulated distribution Figure 2b are shown in the Supporting Information. The fact that our model provides a general expression for the electric field at any point along

the wire as a function of the excitation position, allowing us to model separately the emission at  $z_0$  and  $z = \pm L/2$ , is a distinct advantage. This allows us to directly model the spatially-resolved measurements, as we now detail.

Figure 3a–d displays optical images from the spatially-resolved CL measurements from a  $L = 8.46 \mu\text{m}$  silver nanowire with the SEM image of the wire overlaid. The optical images were taken with a long-pass filter ( $>458 \text{ nm}$ ). To model the spatially-resolved CL emission, we average the simulated CL from a wire of this length at the excitation point and wire ends over the spectral range transmitted by the filter and overlay these curves in Figure 3e,f (with scaling factors and small offsets to coincide more closely with the data, consistent with unknown detector response). Again, there is striking agreement between the simulated curves and the data, validating our physical model. There are small modulations in the simulated curves that are not present in the data. This discrepancy is due to the broad and evanescent nature of the electromagnetic field produced by a fast electron.<sup>[12]</sup> In our 1D model, we considered an ideal point excitation. Modulations in the CL emitted at the point of excitation and ends of the wire would be more prominent if a narrow band-pass, rather than long-pass filter were employed.

### 3. Conclusion

We have derived a 1D electromagnetic model to describe the electron-beam excitation of SPPs and emission of CL from a silver nanowire that has one long-range SPP mode. Our model produces a modulated source amplitude that represents the ability to excite coherent radiative processes at different points along the wire, given that the long-range SPP mode partially reflects at the respective wire end, and influences the energy loss of the electron at the point of excitation. The model captures the essential physics of the interaction between the electron and surface plasmon excitations in the wire and shows strong agreement with both spectrally- and spatially-resolved CL measurements in the SEM. It can be employed to extract the complex SPP wavevector and also the relative excitation probability and phase relationship of the different radiative processes. Our work shows the unique potential for CL in the SEM for obtaining quantitative measurements of nanoplasmonic material parameters and understanding light trapping, SPP excitation/propagation, and light emission in nanowaveguides with more complex geometries and in hybrid structures.<sup>[55,56]</sup>

### 4. Experimental Section

**Materials:** Ethylene glycol (anhydrous,  $>99.8\%$ ), polyvinylpyrrolidone (PVP) ( $M_w = 55\,000$ ), and copper chloride di-hydrate ( $\text{CuCl}_2 \cdot 2\text{H}_2\text{O}$ ) ( $>99.99\%$ ) were purchased from Sigma-Aldrich. Silver nitrate ( $\text{AgNO}_3$ ) (reagent grade) and ethanol (anhydrous, absolute) were purchased from Merck. All chemicals were used without further purification. Ultrapure water (milli-Q,  $18 \text{ M}\Omega$ ) was used.

**Synthesis:** The silver wires were synthesized by modification of a reported procedure.<sup>[40]</sup> All solvents and solutions were initially degassed by bubbling with nitrogen for 20 min prior to use. Degassed ethylene glycol (5 mL) was heated at  $152 \text{ }^\circ\text{C}$  for 1 h under a nitrogen atmosphere.

A solution of  $\text{CuCl}_2 \cdot 2\text{H}_2\text{O}$  in ethylene glycol (0.004 M, 40  $\mu\text{L}$ ) was added to the ethylene glycol at  $152 \text{ }^\circ\text{C}$  and stirred for 15 min. Solutions of PVP (0.147 M, 1.50 mL) and  $\text{AgNO}_3$  (0.094 M, 1.50 mL) in ethylene glycol were then added sequentially to the  $\text{CuCl}_2$  solution. The solution was stirred at  $152 \pm 2 \text{ }^\circ\text{C}$  for 90 min. Upon addition of  $\text{AgNO}_3$  the solution changed from a clear solution to red/orange, then blue/green within 5 to 10 min. Following this, within 2–3 min, the solution turned gray and cloudy/wispy. The dispersion was cooled to room temperature and centrifuged at 3000 rpm for 20 min. The supernatant was removed and the precipitate re-dispersed in ethanol. This washing procedure was repeated twice. Samples were stored in ethanol.

The wires dispersed in ethanol were then deposited onto 50 nm thick silicon nitride membranes (SiMPORE Precision Membrane Technologies) for analysis in the scanning electron microscope (SEM). SEM observation showed they had  $\approx 80 \text{ nm}$  diameters and lengths that ranged from 1.5 to 15  $\mu\text{m}$ .

**Cathodoluminescence:** Spectrally-resolved cathodoluminescence (CL) was performed in a Thermofisher Nova Nanosem 450 (30 keV, 1.6 nA). The CL was collected using a Delmic SPARC system (Andor Shamrock 303i spectrometer, Andor iVac spectral camera, 200 ms dwell times).<sup>[9–11]</sup> Spikes due to cosmic rays were removed using a running box-car median filter. The background from the substrate was subtracted and a system response correction was applied employing the experimental transition radiation spectrum from a gold single crystal specimen.<sup>[12,57]</sup> Corrected spectra were displayed in the Supporting Information. Fits to the total CL intensity profiles as a function of probe position were conducted at intervals of 50 nm in the free space wavelength using the model described in this work (full derivation in the Supporting Information). In the fit, there were twelve parameters. The following six parameters were fixed: the free-space wavevector (in the reflection coefficient  $R$ —see Supporting Information), wire diameter ( $a = 80 \text{ nm}$ ), vacuum permittivity ( $\epsilon_v = 1$ ), permittivity of silver ( $\epsilon_m$ —from tabulated values<sup>[57]</sup>), source strength ( $s_0$ ), and a small quadratic term to account for electron beam scan errors resulting in variation in radial impact parameter. The following six parameters were varied: a linear offset and gradient, an overall amplitude ( $E_T$ ), the complex SPP wavevector ( $k_z$ ), and the relative amplitude and phase of the radiative processes ( $\nu$  and  $\Theta$ , respectively).

Fits were conducted using the Markwardt–Levenberg algorithm implemented in interactive data language.<sup>[58]</sup> Examples of these fits for different wavelengths overlaid on the data are shown in the Supporting Information. The reduced  $\chi^2$  defined as the sum of the squares of the residuals divided by the degrees of freedom ranged from 0.2–0.5 for the ten longest wavelengths, increasing to 1.5–2.0 for the two highest wavelengths, where damping and fewer oscillations made the fit more challenging.

Spatially-resolved CL was performed in a Delmic SECOM installed on a Thermo Fisher Verios 460 (30 keV, 1.6 nA).<sup>[39]</sup> Here the silicon nitride membrane on top of its silicon support was attached to a conductive and transparent ITO-coated coverslip. Optical images (300 ms acquisition time) at different electron probe beam excitation points along the wire were collected using a bottom-mounted optical microscope (40x air objective with a NA of 0.95). A Semrock filter cube DA/FI/TR/Cy5-4X-A-000 was employed with a 458 nm long-pass filter. Fluorescence images were used to find nanowires within the silicon nitride window (see Supporting Information). Dark optical images (Supporting Information) were acquired with the electron beam blanked and subtracted from each image to remove light from the electron emitter that could transmit through the electron column. The CL from electron beam interactions with the silicon nitride support was ten times smaller in magnitude than the CL emitted at the probe excitation point on a wire (Supporting Information). The CL from the glass coverslip was far from the optical focal plane (300  $\mu\text{m}$ ) and would give rise to a constant out-of-focus background. These constant sources of background CL were not considered further as they would not vary as a function of excitation position.

**Pre-Processing:** For the CL spectra, spikes and the background from the substrate were subtracted before the system response function correction was applied. A dark optical image was subtracted from the spatially-resolved CL optical images.

**Data Presentation:** Averaged fitted parameters are shown in Figure 2c–f with the standard error employed as error bars. Error bars in the plot of spatially-resolved CL intensity in Figure 3e employed the standard deviation from three independent Bézier curve profiles. Error bars in Figure 3f show the standard deviation in the average CL from a kernel of five pixels centered on the emission spot, assuming Poisson statistics.

**Sample Size:** Fits were conducted on five (5) silver wires to determine the parameter values displayed in Figure 2c–f.

**Statistical Methods:** Data fits were conducted using the Markwardt–Levenberg algorithm.<sup>[58]</sup>

**Software:** Interactive data language was employed for fitting. Image J was used to extract intensities from the stack of spatially-resolved CL optical images.

## Supporting Information

Supporting Information is available from the Wiley Online Library or from the author.

## Acknowledgements

A.C.Y.L. and T.J.D. contributed equally to this work. The authors acknowledge the use of the instruments and scientific and technical assistance at the Monash Centre for Electron Microscopy, a Node of Microscopy Australia. This research used equipment funded by Australian Research Council grant (LE140100104). A.C.Y.L. acknowledges funding from the Australian Research Council (FT180100594). This work was supported by the Australian Research Council (ARC) through the ARC Centre of Excellence in Exciton Science, CE170100026. A.C.Y.L. and J.E. acknowledge support from the Australian Academy of Technology and Engineering (Global Connections Bridging Grant 414669063). A.C.Y.L. and A.F. acknowledge support from the Science Faculty, Monash University. T.C. and S.H. acknowledge funding from the European Research Council under the European Union's Horizon 2020 research and innovation programme under grant agreement 101017720 (FET-Proactive EBEAM). The authors gratefully acknowledge the use of the SECOM and Thermo Fisher Verios 460 in Imaging Physics at TU Delft and discussions with Jacob Hoogenboom and Pieter Kruit.

Open access publishing facilitated by Monash University, as part of the Wiley - Monash University agreement via the Council of Australian University Librarians.

## Conflict of Interest

T.C. and S.H. are employed by Delmic BV, a company that manufactures instrumentation for cathodoluminescence in the scanning electron microscope.

## Data Availability Statement

Datasets related to this publication are available from the Monash University Figshare repository at <https://doi.org/10.26180/22014383>.

## Keywords

cathodoluminescence, nanowires, scanning electron microscopy, silver, surface plasmon polariton

Received: December 11, 2022

Revised: February 8, 2023

Published online:

- [1] M. Song, D. Wang, S. Peana, S. Choudhury, P. Nyga, Z. A. Kudyshev, H. Yu, A. Boltasseva, V. M. Shalaev, A. V. Kildishev, *Appl. Phys. Rev.* **2019**, 6, 041308.
- [2] M. K. Chen, Y. Wu, L. Feng, Q. Fan, M. Lu, T. Xu, D. P. Tsai, *Adv. Opt. Mater.* **2021**, 9, 2170013.
- [3] P. Khan, G. Brennan, J. Lillis, S. A. M. Tofail, N. Liu, C. Silien, *Symmetry* **2020**, 12, 8.
- [4] C. Schörner, S. Adhikari, M. Lippitz, *Nano Lett.* **2019**, 19, 3238.
- [5] F. Monticone, A. Alú, *Rep. Prog. Phys.* **2017**, 80, 036401.
- [6] S. A. Maier, *Plasmonics: Fundamentals and Applications*, Springer, New York, NY **2007**.
- [7] M. Kociak, L. Zagonel, *Ultramicroscopy* **2017**, 176, 112.
- [8] M. Kociak, O. Stéphan, *Chem. Soc. Rev.* **2014**, 43, 3865.
- [9] E. J. R. Vesseur, J. Aizpurua, T. Coenen, A. Reyes-Coronado, P. E. Batson, A. Polman, *MRS Bull.* **2012**, 37, 752.
- [10] T. Coenen, B. J. M. Brenny, E. J. Vesseur, A. Polman, *MRS Bull.* **2015**, 40, 359.
- [11] A. Polman, M. Kociak, F. J. G. de Abajo, *Nat. Mater.* **2019**, 18, 1158.
- [12] F. J. García de Abajo, *Rev. Mod. Phys.* **2010**, 82, 209.
- [13] A. Howie, *Ultramicroscopy* **2011**, 111, 761.
- [14] R. Carminati, A. Cazé, D. Cao, F. Peragut, V. Krachmalnicoff, R. Pierrat, Y. de Wilde, *Surf. Sci. Rep.* **2015**, 70, 1.
- [15] F. J. García de Abajo, M. Kociak, *Phys. Rev. Lett.* **2008**, 100, 106804.
- [16] N. Kawasaki, S. Meuret, R. Weil, H. Lourenço-Martins, O. Stéphan, M. Kociak, *ACS Photonics* **2016**, 3, 1654.
- [17] V. Myroshnychenko, J. Nelayah, G. Adamo, N. Geuquet, J. Rodríguez-Fernández, I. Pastoriza-Santos, K. Macdonald, L. Henrard, L. Liz-Marzán, N. Zheludev, M. Kociak, F. J. García de Abajo, *Nano Lett.* **2012**, 12, 4172.
- [18] O. Nicoletti, M. Wubs, N. A. Mortensen, W. Sigle, P. A. v. Aken, P. A. Midgley, *Opt. Express* **2011**, 19, 15371.
- [19] D. Rossouw, M. Couillard, J. Vickery, E. Kumacheva, G. Botton, *Nano Lett.* **2011**, 11, 1499.
- [20] D. Rossouw, G. A. Botton, *Phys. Rev. Lett.* **2013**, 110, 066801.
- [21] S. M. Collins, O. Nicoletti, D. Rossouw, T. Ostasevicius, P. A. Midgley, *Phys. Rev. B* **2014**, 90, 155419.
- [22] M. Bosman, E. Ye, S. F. Tan, C. A. Nijhuis, J. K. W. Yang, R. Marty, A. Mlayah, A. Arbouet, C. Girard, M.-Y. Han, *Sci. Rep.* **2013**, 3, 1312.
- [23] D. Schoen, A. Atre, A. García-Etxarri, J. Dionne, M. Brongersma, *Nano Lett.* **2015**, 15, 120.
- [24] G. Beck, *Phys. Rev.* **1948**, 74, 795.
- [25] R. A. Ferrell, *Phys. Rev.* **1958**, 111, 1214.
- [26] H. D. Hattendorff, *Phys. Status Solidi A* **1977**, 42, 1489.
- [27] D. Heitmann, *J. Phys. C* **1977**, 10, 397.
- [28] D. Heitmann, *Opt. Commun.* **1978**, 25, 196.
- [29] N. Yamamoto, A. Toda, *Scanning Microsc.* **1995**, 9, 669.
- [30] E. N. Economou, *Phys. Rev.* **1969**, 182, 539.
- [31] A. Losquin, M. Kociak, *ACS Photonics* **2015**, 2, 1619.
- [32] A. Losquin, L. F. Zagonel, V. Myroshnychenko, B. Rodríguez-González, M. Tencé, L. Scarabelli, J. Förstner, L. M. Liz-Marzán, F. J. García de Abajo, O. Stéphan, M. Kociak, *Nano Lett.* **2015**, 15, 1229.
- [33] J. Zuloaga, P. Nordlander, *Nano Lett.* **2011**, 11, 1280.
- [34] M. Rothe, Y. Zhao, G. Kewes, Z. Kochovski, W. Sigle, P. A. van Aken, C. Koch, M. Ballauff, Y. Lu, O. Benson, *Sci. Rep.* **2019**, 9, 3859.
- [35] M. Kuttge, E. Vesseur, A. Koenderink, H. Lezec, H. Atwater, F. J. García de Abajo, A. Polman, *Phys. Rev. B* **2009**, 79, 113405.
- [36] U. Hohenester, A. Trugler, *Comput. Phys. Commun.* **2012**, 183, 370.
- [37] U. Hohenester, *Comput. Phys. Commun.* **2014**, 185, 1177.
- [38] J. Waxenegger, U. Hohenester, A. Trugler, *Comput. Phys. Commun.* **2015**, 193, 138.
- [39] P. de Boer, J. P. Hoogenboom, B. N. G. Giepmans, *Nat. Methods* **2015**, 12, 503.
- [40] K. E. Korte, S. E. Skrabalak, Y. Xia, *J. Mater. Chem.* **2008**, 18, 437.



- [41] E. S. Barnard, E. J. R. Vesseur, A. Polman, M. L. Brongersma, *Nano Lett.* **2011**, *11*, 4265.
- [42] M. Kuttge, E. Vesseur, A. Polman, *Appl. Phys. Lett.* **2009**, *94*, 183104.
- [43] B. J. M. Brenny, T. Coenen, A. Polman, *J. Appl. Phys.* **2014**, *115*, 244307.
- [44] M. Song, A. Bouhelier, P. Bramant, J. Sharma, E. Dujardin, D. Zhang, G. Colas-des Francs, *ACS Nano* **2011**, *5*, 5874.
- [45] W. Wang, Q. Yang, F. Fan, H. Xu, Z. L. Wang, *Nano Lett.* **2011**, *11*, 1603.
- [46] B. Wild, L. Cao, Y. Sun, B. P. Khanal, E. R. Zubarev, S. K. Gray, N. F. Scherer, M. Pelton, *ACS Nano* **2012**, *6*, 472.
- [47] A. W. Sanders, D. A. Routenberg, B. J. Wiley, Y. Xia, E. R. Dufresne, M. A. Reed, *Nano Lett.* **2006**, *6*, 1822.
- [48] H. Ditlbacher, A. Hohenau, D. Wagner, U. Kreibig, M. Rogers, F. Hofer, F. R. Aussenegg, J. R. Krenn, *Phys. Rev. Lett.* **2005**, *95*, 257403.
- [49] J. D. Jackson, *Classical Electrodynamics*, 2nd ed., John Wiley & Sons Inc, New York **1975**.
- [50] C. Pfeiffer, E. Economou, K. Ngai, *Phys. Rev. B* **1974**, *10*, 3038.
- [51] G. C. Aers, B. V. Paranjape, A. D. Boardman, *J. Phys. F: Met. Phys.* **1980**, *10*, 53.
- [52] K. G. Sullivan, D. G. Hall, *J. Opt. Soc. Am. B* **1997**, *14*, 1149.
- [53] K. Drexhage, *J. Lumin.* **1970**, *1–2*, 693.
- [54] R. Brechbühler, F. Rabouw, P. Rohner, B. Le Feber, D. Poulidakos, D. Norris, *Phys. Rev. Lett.* **2018**, *121*, 113601.
- [55] J. Shi, J. Zhu, X. Wu, B. Zheng, J. Chen, X. Sui, S. Zhang, J. Shi, W. Du, Y. Zhong, Q. Wang, Q. Zhang, A. Pan, X. Liu, *Adv. Optic. Mater.* **2020**, *8*, 2001147.
- [56] J. Chen, Q. Zhang, J. Shi, S. Zhang, W. Du, Y. Mi, Q. Shang, P. Liu, X. Sui, X. Wu, R. Wang, B. Peng, H. Zhong, G. Xing, X. Qiu, T. C. Sum, X. Liu, *Commun. Phys.* **2019**, *2*, 80.
- [57] P. B. Johnson, R. W. Christy, *Phys. Rev. B* **1972**, *6*, 4370.
- [58] C. B. Markwardt, in *Astronomical Data Analysis Software and Systems XVIII* (Eds.: D. A. Bohlender, D. Durand, P. Dowler), Astronomical Society of the Pacific Conference Series, Vol. 411, Astronomical Society of the Pacific, San Francisco **2009**, pp. 251.